Mon. Not. R. Astron. Soc. (2007) doi:10.1111/j.1365-2966.2007.11454.x

Resolved spectroscopy of a gravitationally lensed L^* Lyman-break galaxy at $z \sim 5$

A. M. Swinbank,[1⋆] R. G. Bower,[1] Graham P. Smith,[2,4] R. J. Wilman,[1] Ian Smail,[1] R. S. Ellis,[2] S. L. Morris[1] and J.-P. Kneib[3]

[1]*Department of Physics, Institute for Computational Cosmology, Durham University, South Road, Durham DH1 3LE*
[2]*California Institute of Technology, MC 105-24, Pasadena, CA 91125, USA*
[3]*Laboratoire d'Astrophysique de Marseille, Traverse du Siphon - B.P.8 13376, Marseille Cedec 12, France*
[4]*School of Physics and Astronomy, University of Birmingham, Edgbaston, Birmingham B15 2TT*

Accepted 2006 December 27. Received 2006 December 27; in original form 2006 July 13

ABSTRACT

We exploit the gravitational potential of a massive, rich cluster at $z = 0.77$ to study the internal properties of a gravitationally lensed galaxy at $z = 4.88$. Using high-resolution *Hubble Space Telescope* imaging together with optical (VIMOS) and near-infrared (SINFONI) integral field spectroscopy, we have studied the rest-frame ultraviolet and optical properties of the lensed galaxy seen through the cluster RCS0224−002. Using a detailed gravitational lens model of the cluster, we reconstruct the source-frame morphology on 200 pc scales and find an $\sim L^*$ Lyman-break galaxy with an intrinsic size of only 2.0×0.8 kpc, a velocity gradient of $\lesssim 60\,\mathrm{km\,s^{-1}}$ and an implied dynamical mass of $1.0 \times 10^{10}\,\mathrm{M_\odot}$ within 2 kpc. We infer an integrated star formation rate of just $12 \pm 2\,\mathrm{M_\odot\,yr^{-1}}$ from the intrinsic [O II]λ3727 emission-line flux. The Lyα emission appears redshifted by $+200 \pm 40\,\mathrm{km\,s^{-1}}$ with respect to the [O II] emission. The Lyα is also significantly more extended than the nebular emission, extending over 11.9×2.4 kpc. Over this area, the Lyα centroid varies by less than $10\,\mathrm{km\,s^{-1}}$. We model the asymmetric Lyα emission with an underlying Gaussian profile with an absorber in the blue wing and find that the underlying Lyα emission-line centroid is in excellent agreement with the [O II] emission-line redshift. By examining the spatially resolved structure of the [O II] and Lyα emission lines, we investigate the nature of this system. The model for local starburst galaxies suggested by Mas-Hesse et al. provides a good description of our data, and suggests that the galaxy is surrounded by a galactic-scale bipolar outflow which has recently bursted out of the system. The outflow, which appears to be currently located $\gtrsim$30 kpc from the galaxy, is escaping at a speed of upto $\sim 500\,\mathrm{km\,s^{-1}}$. Although the mass of the outflow is uncertain, the geometry and velocity of the outflow suggests that the ejected material is travelling far faster than escape velocity and will travel more than 1 Mpc (comoving) before eventually stalling.

Key words: gravitational lensing – galaxies: clusters: general – galaxies: high-redshift – galaxies: starburst.

1 INTRODUCTION

One of the most important observational breakthroughs in recent years was the discovery that a significant fraction of high-redshift galaxies are surrounded by 'superwinds' (e.g. Pettini et al. 2002; Shapley et al. 2003; Bower et al. 2004; Wilman et al. 2005) – starburst and/or active galactic nucleus driven outflows which expel gas from the galaxy potential, hence playing no further role in the star formation history of the galaxy. This phenomenon is beginning to be understood by theorists as the missing link in galaxy formation models which are otherwise unable to match the shape and normalization of the luminosity function (Benson et al. 2003; Baugh et al. 2005). These feedback processes may also offer natural explanation as to why only 10 per cent of baryons cool to form stars (the Cosmic Cooling Crisis; White & Rees 1978; Balogh et al. 2001).

However, important questions remain unanswered. Evidence for these superwinds is usually based on observations which compare the nebular emission-line properties with the rest-frame ultraviolet (UV) emission and absorption lines (such as Lyα, Hα and UV interstellar medium (ISM) absorption lines; e.g. Erb et al. 2003). Velocity offsets of several hundred km s^{-1} have been measured, suggestive

⋆E-mail: a.m.swinbank@dur.ac.uk

of large-scale outflows comparable to starburst-driven winds often observed in low-redshift ultraluminous infrared galaxies (ULIRGs) in the local Universe (Martin 2005). However, the current data lack spatial information, which is vital if we are to understand if material escapes into the intergalactic medium (IGM) or whether the outflowing material eventually stalls, fragments and drains back on to the galaxy, potentially disrupting the disc and causing further bursts of star formation.

The key to resolving these issues is to identify similar features in the spatially resolved spectra of distant, young galaxies. However, at the redshifts where these feedback processes are at their peak activity (above $z \sim 2$ i.e. when galaxies were most rapidly forming stars), the immense luminosity distances mean that the emission-line fluxes of these distant galaxies are dramatically reduced. This problem is compounded by the fact that the nebular emission lines (such as [O II], [O III] and Hα) are redshifted into the near-infrared, where the sky background is an order of magnitude brighter than that in the optical. Coupled with the fact that galaxies at these redshifts typically have disc scalelengths of only a few kpc, even with adaptive optics assisted observations on 8–10 m telescopes, only a handful of independent pixels can be recovered from a distant galaxy.

By necessity therefore, above $z \sim 2$ most-detailed studies of individual galaxies have concentrated on the most-luminous (and therefore usually very active and massive) systems (Bower et al. 2004; Swinbank et al. 2005; Wilman et al. 2005), with very few 'normal' galaxies being studied in detail beyond $z = 2$ (Pettini et al. 2002, 2000; Teplitz et al. 2000; Förster Schreiber et al. 2006; Genzel et al. 2006). One way to overcome this problem is to use the deep potential of massive galaxy clusters to boost the flux and sizes of images of distant galaxies which serendipitously lie behind them. This natural magnification provides the opportunity to study intrinsically faint high-redshift galaxies with a spatial resolution that cannot be attained via conventional observations (Smail et al. 1996; Franx et al. 1997; Teplitz et al. 2000; Campusano et al. 2001; Ellis et al. 2001; Smith et al. 2002; Swinbank et al. 2003; Kneib et al. 2004; Swinbank et al. 2006).

The natural magnification caused by the gravitational lens allows us to spatially resolve the morphologies and internal dynamics of galaxies in a level of detail far greater than otherwise possible. For the galaxy discussed in this paper, the amplification factor of 16 corresponds to an increase of over three magnitudes and makes it possible to study the galaxy on independent spatial scales of $\sim$200 pc at $z = 5$. In contrast, without a gravitational lens, 1 arcsec corresponds to 6.5 kpc at $z = 4.88$.

In this paper, we present a VLT/IFU study of the $z = 4.88$ gravitationally lensed galaxy behind the core of the rich lensing cluster RCS0224−002. This galaxy cluster was identified as having a significant concentration of red galaxies in the inner regions by Gladders, Yee & Ellingson (2002). Follow-up spectroscopy confirmed a redshift for the cluster of 0.773 ± 0.0021. The ground-based imaging from Gladders et al. (2002) shows several tangential arc-like structures, many of which resemble images of lensed, background galaxies. One of the most striking of these is a multiply imaged arc approximately 15 arcsec to the north-east of the brightest cluster galaxy (BCG) (see Fig. 1). Follow-up spectroscopy by Gladders et al. (2002) yielded a redshift of $z = 4.88$ from identification of a strong Lyα emission line at 7148 Å.

We concentrate on the dynamics and star-forming properties of the $z = 4.88$ arc observed through the rest-frame UV spectra with the VIMOS IFU and through the nebular ([O II]$\lambda\lambda$3726.1,3728.8 Å) emission-line doublet observed with the SINFONI IFU in the near-infrared. The IFU data provide a two-dimensional map of the galaxy's properties in sky coordinates. In order to interpret this map, we must correct for the magnification and distortion caused by the lensing potential using a mass model for the cluster lens. This model is constrained by requiring it to account for the positions and

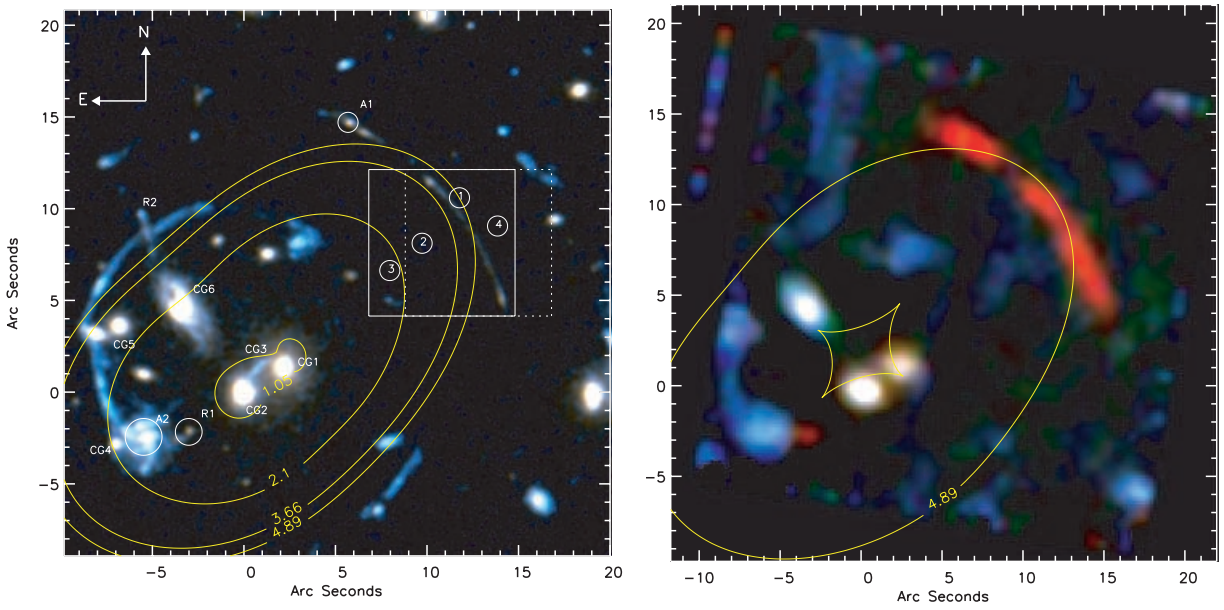

Figure 1. Left-hand panel: true colour *HST VI*-band image of the core of the lensing cluster RCS0224−002 at $z = 0.78$. The contours mark the high-redshift critical curves (curves of infinite magnification) from the gravitational lens model described in Section 3. We also overlay the field of view of the SINFONI IFU (shown by the white box) which was used to map the [O II]λ3727 emission. The cluster galaxies which we are able to spectroscopically identify are labelled CG1–6. R1 is the radial counter-image of the $z = 4.88$ arc and R2 is the $z = 1.05$ radial arc from Sand et al. (2005). Serendipitous background galaxies are labelled A1 and A2 (VIMOS) and 1–4 (SINFONI) (see Appendix A). Right-hand panel: *VR*(*I*+Lyα) colour image of the cluster core generated from the VIMOS IFU data cube. The inner and outer curves show the $z = 4.88$ caustic and critical curves, respectively. The centre of the cluster (0,0) is at $\alpha = 02{:}24{:}34.255$ $\delta = -00{:}02{:}32.39$ (J2000) and we have rotated and aligned the *HST* and VIMOS data such that north is up and east is to the left-hand side in both panels.

redshifts of the gravitationally lensed arcs in the cluster. The lensing model then allows us to determine the source-plane morphology and geometry of the continuum and line emission we use.

The structure of this paper is as follows. In Section 2, we present the data on which this paper is based: a combination of *Hubble Space Telescope* (*HST*), ground-based imaging, and integral field spectroscopy obtained with the SINFONI and VIMOS IFUs on the VLT. In Section 3, we present the source-plane properties of the arc and the spatially resolved spectroscopy and in Sections 4 and 5 we present our discussion and conclusions, respectively. Throughout this paper, we use the Vega magnitude system and assume a cosmology with $H_0 = 72\,\mathrm{km\,s^{-1}}$, $\Omega_0 = 0.3$ and $\Lambda_0 = 0.7$.

2 OBSERVATIONS AND DATA REDUCTION

2.1 *HST* imaging

HST WFPC2 I_{814}- and V_{555}-band observations of the lensing cluster RCS0224−002 were obtained from the *HST* public archive.[1] The I_{814}- and V_{555}-band observations were 10.5 and 8.4 ks, respectively, and the data were reduced using the standard STSDAS package in IRAF. The resulting image (Fig. 1) covers the brightest central cluster galaxies and the target arc at a resolution of 0.0996 arcsec pixel^{-1}. From the *HST* imaging, the $z = 4.88$ arc is red ($V_{606} - I_{814} = 1.7 \pm 0.1$) with an average surface brightness of $\mu_{I_{814}}$=25.0 and an integrated magnitude of $I = 22.2$.

2.2 VIMOS Integral Field Spectroscopy

The $z = 4.88$ arc was observed with the VIMOS IFU (LeFevre et al. 2003) for a total of 43.2 ks (split into 16 × 2700 s exposures) between 2004 December 16 and 2005 December 12 in $\lesssim$0.6 arcsec seeing and photometric conditions. We used the MR-orange grism which results in a field of view of 27 × 27 arcsec^2 at 0.67 arcsec pixel^{-1} and a spectrum resolution of $\lambda/\Delta\lambda \sim 1100$ at 7000 Å. To reduce the data, we used the VIMOS ESOREX pipeline which extracts, wavelength calibrates and flat-fields the data. The final data cubes cover a wavelength range of 5000–11 000 Å and has a resolution of 6.6 Å full width at half-maximum (FWHM) (measured from the width of the sky-lines at a wavelength of 7150 Å). In all future sections, linewidths are deconvolved for instrumental resolution. Flux calibration was achieved by using observations of ESO standard stars. These observations were taken either immediately before, or immediately after the science observations and were reduced in an identical manner. Since there are no point sources in our data cubes, we measure the seeing from the standard stars in the collapsed data cubes and derive typical seeing measurement of ∼0.8 arcsec at a typical airmass 1.1. During the standard star observation, the ESO seeing monitor registered median seeing of 0.7 arcsec – hence, we conservatively assume that the VIMOS IFU observations were taken in 0.8-arcsec seeing.

[1] PID: 9135: obtained from the Multimission Archive at the Space Telescope Science Institute (MAST). The Space Telescope Science Institute is operated by the Association of Universities for Research in Astronomy, Inc., under NASA contract NAS5-26555. Support for the MAST for non-*HST* data is provided by the NASA Office of Space Science via grant NAG5-7584 and by other grants and contracts.
PID: 207254: based on observations taken with the *Spitzer Space Telescope*, which is operated by the Jet Propulsion Laboratory, California Institute of Technology under NASA contract 1407.

After reducing each of the observations to a data cube, we construct and apply a master flat-field in order to correct for the fringing effects which are particularly prominent above 8000 Å. In each of the (spatially dithered) data cubes, we construct a broad-band image by collapsing the data cube in wavelength between 6000 and 7500 Å after the brightest objects. We then apply this mask to every wavelength and stack the resulting data cube (without spatial offsets and ignoring masked pixels). This produces a 'master-flat-field' which is then divided into each of the science observations to reduce the effects of the fringing. These individual data cubes are then sky-subtracted by masking the brightest objects in the individual frames and constructing a sky-spectrum by collapsing the data cube in both spatial dimensions (since the four quadrants of the VIMOS IFU have slightly different throughputs, we note that the sky-subtraction was performed quadrant-by-quadrant). To build the final data cube, we create broad-band images from each data cube and cross correlate these in order to spatially align and create the final mosaic. The final data cube is created using an average with a 3σ clip to reject cosmic rays.

In Fig. 1, we show a colour image of the cluster and arc, generated from the data cube. We generate three colours from the data cube by collapsing the data cube between 5000–6000 Å, 6000–7000 Å and 7000–8000 Å as blue, green and red, respectively.

2.3 SINFONI IFU observations

To map the nebular emission-line properties of the $z = 4.88$ arc, we used the SINFONI IFU (Eisenhauer et al. 2003). At $z = 4.88$, the [O II]λλ3726.1, 3728.8 emission-line doublet is redshifted to 2.19 μm and into a stable part of the *K* band relatively free from strong OH airglow emission. The SINFONI IFU uses an image slicer and mirrors to reformat a field of 10 × 10 arcsec^2 at a spatial resolution of 0.25 arcsec pixel^{-1}. We used the HK grating which results in a spectral resolution of $\lambda/\Delta\lambda = 1700$ at 2.20 μm (the sky-lines have a resolution 13 Å FWHM at this wavelength) and covers a wavelength range of 1.451–2.463 μm. In all future sections, emission linewidths are deconvolved for the instrumental resolution. To observe the target, we used ABBA chop sequences; however, since the arc only filled one-half of the data cube, we chopped 2 arcsec west to sky (see Fig. 1), thus keeping the object inside the IFU. We observed the target for a total of 43.2 ks (split into 16 × 2700 s exposures) between 2005 August 10 and 2005 September 28 in $\lesssim$0.6″ seeing and photometric conditions. Individual exposures were reduced using the SINFONI ESOREX data-reduction pipeline which extracts, flat-fields, wavelength calibrates and forms the data cube. The final data cube was generated by aligning the individual data cubes and then combining the using an average with a 3σ clip to reject cosmic rays. For flux calibration, standard stars were observed each night during either immediately before or immediately after the science exposures. These were reduced in an identical manner to the science observations. In Figs 2 and 3, we show both the one-dimensional spectrum of the arc (generated by collapsing the data cube over the object in both spatial domains) and the narrow-band image of the arc generated by collapsing the data cube in the wavelength direction over the [O II] emission line.

3 ANALYSIS AND RESULTS

3.1 Mass modelling

Reconstruction of the intrinsic properties of the galaxy at $z = 4.88$ requires removal of the gravitational magnification from the

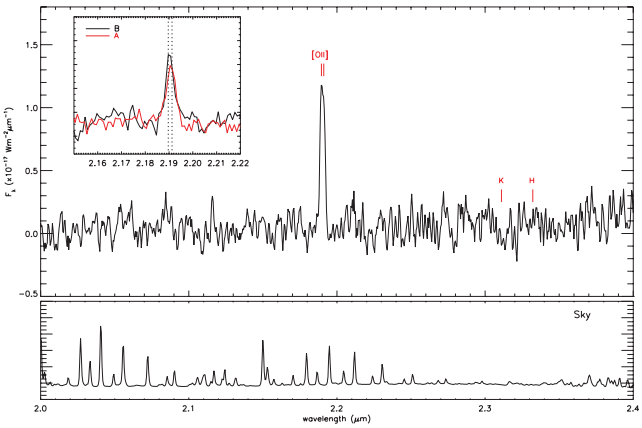

Figure 2. Collapsed, one-dimensional spectrum of the arc from our SINFONI IFU observations. The [O II] emission line has a redshift of 4.8757 ± 0.0005 and a linewidth of $\sigma = 180 \pm 30\,\mathrm{km\,s^{-1}}$. The inset shows the renormalized [O II] emission lines for the two regions (A and B) shown in Fig. 4. We also show a sky-spectrum (below) for comparison (scaled in flux for clarity).

observables. We therefore use the four spectroscopically confirmed images of the $z = 4.88$ galaxy to constrain a model of the mass distribution in the cluster. These four images comprise the three images in the tangential arc identified by Gladders et al. (2002) and the fourth image identified via our integral field spectroscopy (Appendix A). The candidate radial arc at $z = 1.05$ (A3 in Fig. 1; Sand et al. 2005) and the object identified at $z = 3.66$ adjacent to the $z = 4.88$ arc (A1 in Fig. 1) appear not to be multiply-imaged, and so are not included as constraints. The configuration of the four observed images and the lack of strong radial amplification of the fourth image implies that the fifth image lies very close to the centre of the cluster mass distribution. We therefore expect the fifth image to be strongly de-magnified and thus likely undetectable in the current data. We identify the dense knot of emission in each of the four observed images as being images of the same underlying region of the galaxy, and use the position of these knots to constrain the model. Following appendix A of Smith et al. (2005), the number of constraints is therefore $n_C = 6$.

The central region of RCS0224 contains two bright elliptical galaxies: CG1 and CG2 (Fig. 1) – we therefore construct a three-component model comprising the cluster-scale mass distribution (dark matter and gas), CG1 and CG2. We parametrize all three mass components as truncated pseudo-isothermal elliptical mass distributions, each described by the following parameters: $\{x, y, \epsilon, \theta, r_{\rm core}, r_{\rm cut}, v_{\rm disp}\}$ (Kassiola & Kovner 1993; Kneib et al. 1996) – that is, 21 parameters in total, comprising the centre, ellipticity, position angle, core radius and cut-off radius of each mass component. To obtain a well-constrained model (and given the number of constraints above: $n_C = 6$), we prefer no more than six out of these 21 parameters to be free parameters in the lens model. The geometrical parameters (x, y, ϵ, θ) describing CG1 and CG2 are therefore matched to their two-dimensional light distributions, and their respective $r_{\rm core}$ and $r_{\rm cut}$ parameters are matched to the shape of the light profile of each galaxy. Finally, the mass-to-light ratio of each galaxy is fixed by matching their velocity dispersions to the measured velocity dispersion (Table B1). Turning to the parameters describing the cluster-scale mass, we fix both $r_{\rm core}$ and $r_{\rm cut}$ at 75 kpc and 1 Mpc, respectively. The former value is representative of massive clusters, and our decision to fix this parameter is caused by the non-detection

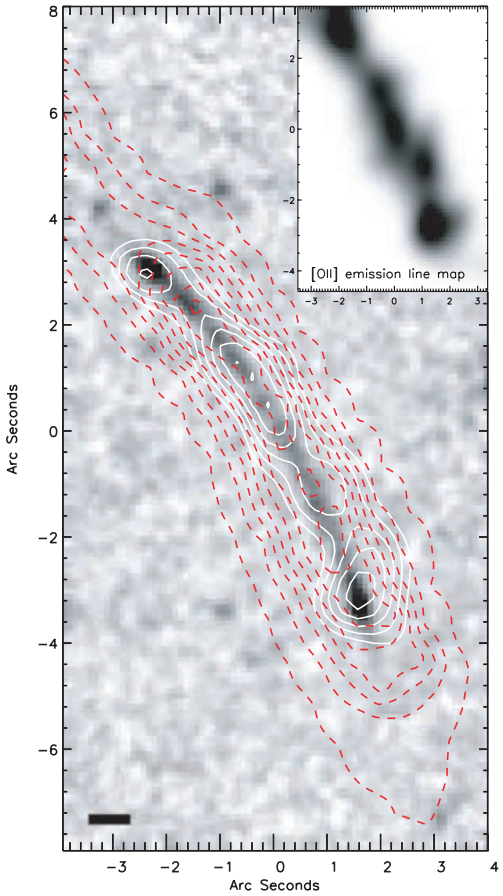

Figure 3. Image-plane observations of the $z = 4.88$ arc: *HST* continuum (grey-scale), Lyα emission (red contours online) and [O II] emission (white contours). The image shows that the Lyα emission is much more extended than either the [O II] or the continuum morphology. The solid bar in the bottom left-hand corner represents the 0.8-arcsec seeing disc for both the VIMOS and SINFONI IFU observations. Inset: continuum-subtracted, narrow-band image around the redshifted [O II]λ3727 emission of the arc from our SINFONI IFU observations. The highest surface brightness components in both the optical image and the [O II] emission-line map are well matched, though the [O II] emission-line map also shows that the highly sheared component has more structure than evident in the optical imaging.

of the central fifth image of the $z = 4.88$ arc. The lack of the fifth image reduces our ability to constrain the radial shape of the mass distribution within the tangential critical curve. We also run models with $r_{\rm core} = 50$ and 100 kpc to confirm that the final results are not altered by the adopted value of $r_{\rm core}$. For completeness, we include the result of this check in the error on the lens magnification calculated below. Fixing $r_{\rm cut} = 1$ Mpc is motivated by the small field of view of the *HST* data and within those data the small angular scale subtended by the strong lensing constraints. We are therefore unable to constrain this parameter, but our results are insensitive to its value. In summary, we therefore fit a model with five free parameters to the data. The free and fixed parameters are listed in Table 1.

All of the lens modelling is performed using the LENSTOOL software (Kneib 1993; Kneib et al. 1996), incorporating a Markov Chain Monte Carlo (MCMC) sampler (Jullo et al., in preparation). The model parameters with the lowest χ^2 found with this MCMC approach and 68 per cent confidence intervals around these parameters values after marginalizing over the other four parameters in each

Table 1. Gravitational lens model parameters.

	Δ RA (arcsec)	Δ Dec. (arcsec)	ϵ	θ (°)	$r_{\rm core}$ (kpc)	$r_{\rm cut}$ (kpc)	$v_{\rm disp}$ (km s^{-1})
Dark matter halo	-0.6 ± 1.6	2.1 ± 1.4	0.18 ± 0.02	-49 ± 5	[75]	[1000]	935 ± 30
CG1	[0.0]	[0.0]	[0.07]	[169]	[0.2]	[42]	[230]
CG2	[2.4]	[− 1.2]	[0.11]	[202]	[0.2]	[38]	[220]

Note. Numbers in square brackets are fixed in the fit. Position angles are clockwise from north.

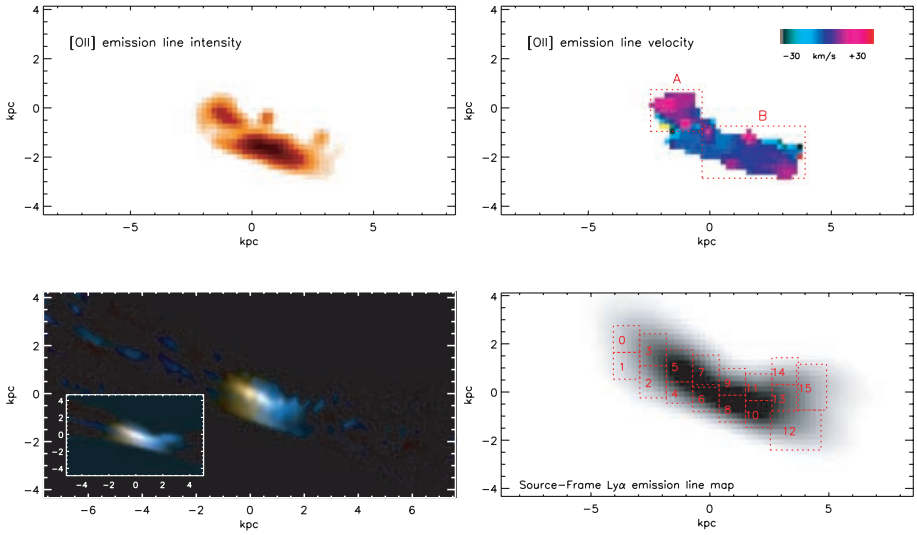

Figure 4. Source-plane observations of the $z = 4.88$ galaxy from the *HST*, VIMOS and SINFONI observations. Top left-hand panel: [O II] emission-line intensity of the galaxy (dark regions represent regions of highest intensity). Top right-hand panel: [O II] emission-line velocity structure of the galaxy which shows a maximum velocity shift of 60 ± 20 km s^{-1} along the long axis of the galaxy. Bottom left-hand panel: reconstructed true colour *HST VI* image of the $z = 4.88$ arc. Inset: reconstructed *HST* image after a smoothing scale of 0.8 arcsec has been applied to the sky-plane image. Bottom right-hand panel: reconstructed Lyα emission-line map of the $z = 4.88$ arc. The boxes show regions from which the spectra in Fig. 6 were extracted.

case, are listed in Table 1, and we show the critical curve of the best-fitting model in Fig. 1. The lens model predicts the fifth image to lie at the centre of CG1 and to be very faint $-R \gtrsim 36$, that is, de-magnified by ∼14 mag relative to the tangential arc. Although the model makes a clear prediction for the location of this image, it is clearly too faint to detect with the available data. We ray-trace the $z = 4.88$ galaxy through the family of models within the 68 per cent confidence surface in the five-dimensional parameter space to compute the mean, luminosity-weighted magnification of $\mu = 16 \pm 2$ (which corresponds to $\Delta m = 3.0 \pm 0.2$ mag).

Accounting for the lensing magnification, the intrinsic magnitude of this galaxy is $I = 25.2$. In comparison, deep imaging surveys of Lyman-break galaxies (LBGs) at $z \sim 5$ have derived an L^* of $i \sim 25.3$ (Ouchi et al. 2004). This suggests that the $z = 4.88$ galaxy is typical of the UV continuum selected LBG population at this redshift. In Fig. 4, we show the reconstructed *HST* image of the galaxy. In the source-plane the galaxy has an FWHM of only 2.0 × 0.8 kpc, and indicates a flattened (or bar-like) geometry. Such an elongated morphology is not unusual for galaxies at these redshifts: in a recent high-resolution imaging survey of LBGs at $z > 2.5$ with the *HST*, Ravindranath et al. (2006) concluded that up to 50 per cent of LBGs show evidence for bar-like morphologies (with mean scalelengths of 1.7–2.0 kpc). Thus, the galaxy appears typical in terms of its source-plane morphology, brightness and size of the population at $z \sim 5$.

3.2 Spatially resolved spectroscopy

3.2.1 Nebular emission

By fitting a double Gaussian profile of fixed separation (corresponding to the redshifted separation of the doublet) and intensity but variable width, redshift and intensities of the doublet to the collapsed spectrum, the [O II] emission yields a systemic redshift of 4.8757 ± 0.0010 and and intrinsic width of $\sigma = 100 \pm 20$ km s^{-1} (in the rest frame of the galaxy). We assume that the [O II] maps the systemic redshift and all velocities are given with respect to this value. The integrated emission-line flux of $5 \pm 1 \times 10^{-20}$ W m^{-2} suggests a star formation rate (SFR) (corrected for lensing amplification, but uncorrected for reddening) of $12 \pm 2\,{\rm M}_{\odot}$ yr^{-1} (assuming the calibration of L([O II]) to SFR given in Kennicutt 1998).

In Fig. 2, we show the intensity distribution and collapsed spectrum of the [O II] emission. Intensity and velocity maps were derived by fitting the [O II] emission-line doublet in each 0.25 arcsec pixel using the same technique described above. We used a χ^2 minimization procedure, taking into account the greater noise of at the positions of the sky-lines. In cases where the fit failed to detect the line, the region was increased to 2 × 2 pixels (0.5 × 0.5 arcsec^2). Using a continuum fit, we required a minimum signal-to-noise ratio (S/N) of 3 to detect the line, and when this criterion is met, we fit the [O II] emission-line doublet with a Gaussian profile of fixed

separation allowing the central wavelength and normalization to vary. In Fig. 4, we show the intensity distribution and velocity structure of the [O II] emission-line flux.

It is clear that the brightest components in the rest-frame UV are also the brightest in the [O II] emission. In the source plane, we find that the easternmost component is marginally redshifted relative to the western component. Relative to the combined spectrum, the eastern region has $v = -20 \pm 20\,\mathrm{km\,s^{-1}}$ (with a velocity dispersion of $\sigma = 80 \pm 18\,\mathrm{km\,s^{-1}}$), while the western component is at $+20 \pm 15\,\mathrm{km\,s^{-1}}$ (and a velocity dispersion of $85 \pm 12\,\mathrm{km\,s^{-1}}$). The quoted uncertainty here is dominated by possible variations in the [O II] doublet line ratios, which was left free in these fits.

Since the [O II] velocity dispersion (σ) reflects the dynamics of the gas in the galaxies' potential well, we estimate the dynamical mass of the galaxy. Following the same prescription of Erb et al. (2006), we use the velocity dispersion and spatial extent of the [O II] flux to infer a dynamical mass of $\sim 1 \times 10^{10}\,\mathrm{M_\odot}$ within a radius of 2 kpc. Clearly this mass has large uncertainties since the mass depends on the mass density profile, velocity anisotropy and relative contributions to σ from random motions or rotation and possible differences between the total mass and that of the tracer particles used to measure it. Nevertheless, it is worth noting that the mass we derive is a factor of $\sim 5\times$ smaller than the median dynamical mass of $z \sim 3$ LBGs from Erb et al. (2006) measured in exactly the same way.

3.2.2 *Lyman α*

In Fig. 4, we show the reconstructed source-plane Lyα morphology of the arc. It is immediately apparent that in the source-plane, the Lyα is more extended than the [O II], or the continuum light, extending over 11.9 × 2.4 kpc (FWHM). Fig. 5 shows the collapsed spectrum of the arc overlaid with the expected position of the Lyα emission line for the systemic redshift. (We also mark the expected position of the UV ISM lines which lie in regions of the sky free from strong OH airglow emission.) The integrated Lyα line flux is $3.7 \pm 0.5 \times 10^{-15}$ erg s^{-1} cm^{-2}, corresponding to an SFR of $5 \pm 2\,\mathrm{M_\odot\,yr^{-1}}$ (unlensed). In comparison, the 1500-Å continuum flux suggests an SFR of $3 \pm 2\,\mathrm{M_\odot\,yr^{-1}}$ (Kennicutt 1998).

From the collapsed spectrum of the galaxy, we measure a redshift from the centroid of the Lyα emission line and measure a velocity offset from the systemic redshift of $+200 \pm 40\,\mathrm{km\,s^{-1}}$. Velocity offsets of this magnitude between Lyα and nebular emission lines (such as [O II] or Hα) are a common feature of galaxies at $z \sim 3$ (Erb et al. 2003; Shapley et al. 2003). In both the collapsed spectrum (Fig. 5) and the spatially resolved spectra (Fig. 6), the strong Lyα from the galaxy shows an asymmetric profile in which the blue wing of the Lyα is absorbed, presumably giving rise to the apparent redshift offset between the [O II] and Lyα. It is also clear that there is an extended wing of emission in the red side of the line.

Asymmetry in the Lyα emission-line spectra of LBGs at $z \sim 2$–3 is common and often gives rise to velocity offsets of several hundred km s^{-1}. These velocity offsets are usually attributed to galactic-scale outflows, presumably powered by supernovae. However, since the optical depth of the Lyα forest is an order of magnitude larger at $z = 5$ than at $z = 3$, (where most spectroscopic studies have taken place), we first investigate whether the IGM could cause the absorption in the blue wing of the emission line.

At $z = 5$ the mean optical depth of the Lyα forest is 1.7 ± 0.2 (Fan et al. 2006) which corresponds to a transmitted flux of 20 per cent. We therefore investigate whether the Lyα profile could be explained

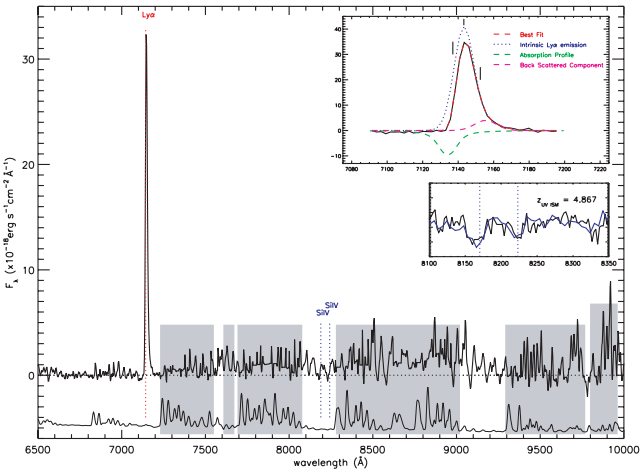

Figure 5. Collapsed, one-dimensional spectrum of the arc from our VIMOS IFU observations. The dashed vertical lines show the expected position of the UV emission and absorption lines for the systemic redshift of $z = 4.8757$ (as measured from the [O II] emission line). The Lyα emission appears redshifted with respect to the systemic velocity, and has an asymmetric line profile. We also detect the weak UV ISM lines of Si IV. These lie in a region devoid of strong sky emission. The hashed regions show regions of strong sky emission and the horizontal dashed line marks a continuum level of zero. Top inset: the Lyα emission line with the model described in Section 3.2.2. The black (solid) line shows the observed spectra. The asymmetric line is best fitted with an underlying Gaussian emission-line profile (blue-dotted line online) combined with a Voigt profile absorber (green-dashed line online) and a third Gaussian which accounts for the red wing of emission. Whilst the observed Lyα emission appears redshifted from the systemic velocity, the best-fitting underlying emission profile has a centroid in excellent agreement with the [O II] emission. Lower inset: spectra around the rest-frame UV absorption lines Si IV$\lambda\lambda$1393.76,1402.8. We overlay the best-fitting template (blue online) from Shapley et al. (2003) and use this to infer a velocity shift of $-400 \pm 100\,\mathrm{km\,s^{-1}}$ from the systemic redshift.

as the result of average IGM absorption, or whether the absorption needed to be due to material associated with the lensed galaxy. The mean optical depth is measured by averaging the absorption of individual clouds on scales of 6000 km s^{-1} (6 Mpc comoving). We fit the Lyα emission line with an underlying Gaussian emission-line profile (centred on the systemic redshift of the galaxy as measured from the [O II] emission), convolved with a step function which models the average IGM (all profiles are then convolved with the instrumental resolution). We also include a broad Gaussian emission-line profile (also centred at the systemic redshift) to account for the extended red wing of emission. Allowing the redshift of the IGM component to vary, we find that an acceptable match emission-line shape is best matched when the IGM step function is placed between -80 and $+10\,\mathrm{km\,s^{-1}}$ from the galaxy (between -85 and $+10$ kpc comoving for out adopted cosmology). This is inconsistent with our assumption of a large-scale average absorption, implying that the absorption we see results from an individual cloud (or clouds) lying close to the target galaxy.

Moreover, a simple step function fails to adequately reproduce the line shape of the blue wing. A better fit is obtained if the line shape is instead modified by a single absorbing cloud. We model the emission profile by Gaussian profile combined with a Voigt profile absorber in the blue wing. In this fit, the wavelength of the underlying best-fitting Gaussian profile (blue dotted line in Fig. 5) was allowed to vary, but the fitted centroid at 7143.0 ± 0.5 Å ($z = 4.8758 \pm 0.0001$) is in excellent agreement with the nebular emission-line

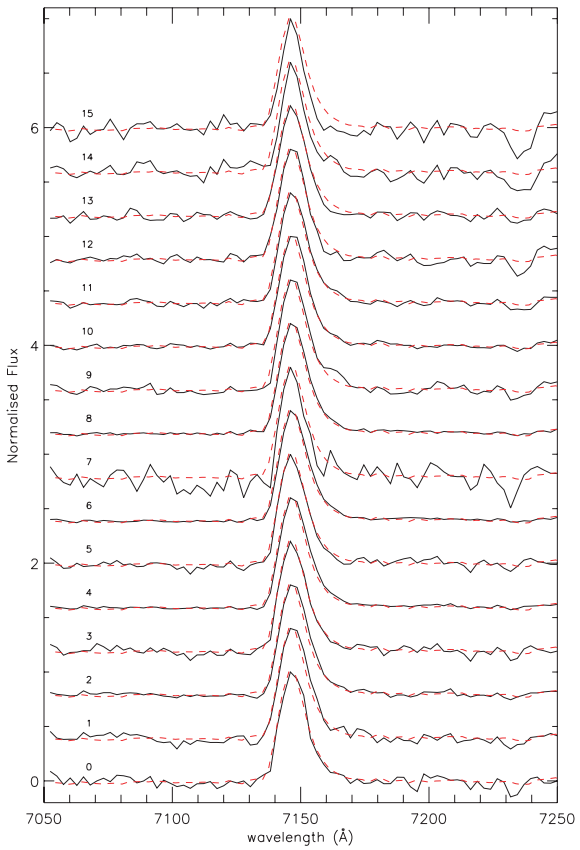

Figure 6. One-dimensional spectra around the redshifted Lyα emission from the $z = 4.88$ galaxy from the 15 regions shown in Fig. 4 (black online). Each of the spectra has the composite spectra (scaled) and overlaid for comparison (red-dashed line). The Lyα emission in all of the spectra shows an asymmetric profile, with the blue wing of the Lyα emission truncated making it to appear redshifted by $+200 \pm 40\,\mathrm{km\,s^{-1}}$ from the nebular ([O II]) emission line. Furthermore, the centroid of the Lyα emission varies by less than $10\,\mathrm{km\,s^{-1}}$ (rest) across the whole galaxy image.

redshift as measured from [O II]. This underlying Gaussian profile also has a width of $\sigma = 4.8$ Å ($\sigma = 200\,\mathrm{km\,s^{-1}}$ in the rest frame of the galaxy). The absorber in the blue wing of the Lyα emission (green dashed line) has a centroid of 7138.0 ± 0.1 Å ($z = 4.8717 \pm 0.0001$, or $\Delta v = -500\,\mathrm{km\,s^{-1}}$ relative to the intrinsic emission) and a width of $\sim 100\,\mathrm{km\,s^{-1}}$. Since the flux in the Voigt profile reflects the column density of the neutral gas, we infer $N_{\mathrm{H\,I}} = 1.6^{+2.5}_{-1.1} \times 10^{19}\,\mathrm{cm^{-2}}$ and $\sigma = 110 \pm 50\,\mathrm{km\,s^{-1}}$. The large uncertainties in the value of $N_{\mathrm{H\,I}}$ and σ reflect the fact that the inferred value of $N_{\mathrm{H\,I}}$ lies between the flat and linear part of the curve of growth for hydrogen.

With this two-component model, we are able to fit the asymmetry in both the collapsed and the spatially resolved spectra. However, even with two components there remains excess flux in the red wing of the emission line. To compensate for this emission, we also fit a third Gaussian profile component in the red wing, again allowing the redshift, width and intensity to vary. The improvement between the three fit and two fit models is $\Delta\chi^2 = 12$–38 (~ 3–6σ; depending on whether we fit the individual spectra or the combined spectrum). The best-fitting model therefore includes a third component with a redshift centroid at 7153.44 ($z = 4.8860$) and a width of $\sigma = 260\,\mathrm{km\,s^{-1}}$. The velocity offsets of the three components are summarized in Table 2. As we discuss in Section 4, this third component may naturally arise from Lyα photons back-scatter on the interior of an outflowing shell. Thus the best-fitting model to the asymmetric Lyα emission is one in which the Lyα photons are generated in similar regions (and at the same redshift) as the [O II], but the emission profile is modified by foreground neutral material. This foreground material absorbs/scatters photons from the blue wing of the line, causing an apparent redshift offset between the nebular emission and Lyα.

The description of the line profile given above is typical of the emission profile seen in other LBGs. The key advantage of observing the lensed system is that we are able to spatially resolve the emission line, and hence investigate the spatial variations in the absorption and emission. We divide the IFU data cube into the spatial regions shown in Fig. 4. For reference these have been labelled 0–15. The resulting spectra are shown in Fig. 6. The most-striking feature of this figure is that (apart from variations in intensity) the line profile appears remarkably constant across the galaxy. For each spatial element, we measure the centroid of the emission and find that the intrinsic emission-line centroid varies by less than $10\,\mathrm{km\,s^{-1}}$ (rest frame) across the whole galaxy image. (This value was derived by fitting both the two- and the three-component models above.) Indeed, as Fig. 6 shows, the asymmetry in the Lyα profile is evident across the whole galaxy. Applying a free fit, each of the individual spectra is consistent with the mean, with the maximum $\Delta\chi^2 = 1.3$ (and an average $\Delta\chi^2 \sim 0.5$). From the position of the Voigt absorber, we also note that the blue-edge of the emission line cuts off at a wavelength corresponding to variations of less than $20\,\mathrm{km\,s^{-1}}$ at a redshift of 4.8717 ± 0.0001. This constancy in the line shape and centroid across the galaxy image is discussed further below.

3.2.3 UV absorption

In the integrated rest-frame UV continuum spectrum of the galaxy, we also detect the weak Si IV($\lambda\lambda$1393, 1402.77) absorption features. Whilst these are very weak in our spectra (the S/N in continuum in regions free from strong sky emission is only ~ 3), the separation

Table 2. Properties of the emission and absorption lines.

Component	z	$66\Delta v$ ($\mathrm{km\,s^{-1}}$)	σ ($\mathrm{km\,s^{-1}}$)	v_{shear} ($\mathrm{km\,s^{-1}}$)
[O II]	4.8757[5]	0	100 ± 30	$-30 < v < 30$
Lyα (principle)	4.8760[5]	$+20 \pm 50$	230 ± 40	$\lesssim 20$
Lyα (red wing)	4.8860[15]	$+520 \pm 150$	260 ± 80	$\lesssim 50$
Lyα (blue absorption)	4.8680[10]	-500 ± 100	110 ± 30	$\lesssim 20$
Si IV absorption	4.8700[10]	-400 ± 100	~ 480	$\lesssim 150$

Notes. The value given in the z column is the error in the last decimal place. v_{shear} denotes the maximum velocity gradient/shear in the given emission/absorption line.

between the doublet is 9.80 ± 0.15 Å (rest), which is in excellent agreement with the expected value of 9.77. To calculate the redshift of these absorption lines, we cross-correlate the spectrum around 8200 Å with the rest-frame UV composite spectrum of LBGs from Shapley et al. (2003) and find that these absorption lines are blueshifted by $-400 \pm 100\,\mathrm{km\,s^{-1}}$ ($z = 4.870 \pm 0.0007$) from the systemic redshift as defined by the [O II] emission line (Fig. 5). It is worth noting that in the LBG composite spectrum from Shapley et al. (2003) the interstellar absorption features (O Iλ1303+SiIIλ1260) are detected with a significance similar to that of Si IV. However, at $z = 4.88$, these are redshifted to 7656 Å and into the middle of the Frauenhoffer *A* band and are therefore not expected to be detected.

The observed velocity offsets between the nebular ([O II]), Lyα and UV ISM lines are therefore consistent with the situation seen in most high-redshift LBGs where velocity offsets of several hundred $\mathrm{km\,s^{-1}}$ have been measured (e.g. Erb et al. 2003; Steidel et al. 2004). These velocity offsets are attributed to starburst-driven superwinds and we base much of our interpretation on this model.

4 DISCUSSION

Before attempting to interpret the observations, we briefly review the results of the observations. The [O II] emission maps the star-forming regions, which appear to have an elongated (bar-like) morphology with a spatial extent of only 2.0×0.8 kpc, which appears to contain all the stars in the galaxy. We use the [O II] emission to infer a systemic redshift of 4.8757 ± 0.0005. Using the [O II] emission, we infer an integrated SFR of $12 \pm 2\,\mathrm{M_\odot\,yr^{-1}}$ (Kennicutt 1998) and the spatial extent and linewidth of [O II] suggest a dynamical mass of $\sim 1 \times 10^{10}\,\mathrm{M_\odot}$ within 2 kpc. Turning to the rest-frame UV spectrum, the Lyα emission is much more extended than that of [O II], extending over 11.9×2.4 kpc (i.e. at least a factor of 4× the spatial extent of [O II]). Moreover, the peak of the Lyα emission is redshifted by $+200 \pm 40\,\mathrm{km\,s^{-1}}$ from [O II]. Across the whole spatial extent, the Lyα emission-line centroid varies by less than $10\,\mathrm{km\,s^{-1}}$ (rest frame) and the line profile is remarkably constant over the same spatial extent. The Lyα emission (both in the collapsed spectrum and in the spatially resolved) has an asymmetric profile which is best explained by a three-component model. The underlying Gaussian emission-line profile has a centroid in excellent agreement with the nebular emission, an absorber which is blueshifted by $-500 \pm 100\,\mathrm{km\,s^{-1}}$ from the systemic redshift and an extended 'red wing' of emission is redshifted by $+520 \pm 150\,\mathrm{km\,s^{-1}}$. Finally, the UV ISM lines of Si IV are blueshifted by $-400 \pm 150\,\mathrm{km\,s^{-1}}$ from the systemic redshift, although it has not been possible to derive any spatial information across the galaxy from these weak lines.

4.1 A starburst with a bi-conical outflow?

The observed velocity offsets between the [O II], Lyα and UV ISM lines in RCS0224arc are consistent with situation seen in most high-redshift LBGs in which the presence of 'superwinds' (driven by the collective effects of star formation and supernovae) naturally explains the observations. Our spatially resolved spectra therefore offer us the opportunity to study the spatial structure and energetics of the outflowing material in this galaxy.

With the spatially resolved emission and absorption line velocities and line profiles in hand, we can begin to build a coherent picture of the properties of the $z = 4.88$ galaxy behind RCS0224. The star-forming regions in this galaxy appear to have an elongated bar-like morphology which contains all the stars in the galaxy. The dynamics of the [O II] emission do not require regular disc-like rotation, and we place a limit of less that $60\,\mathrm{km\,s^{-1}}$ (in projection) on the velocity shear. From the spatially integrated line profile, the width of the [O II] emission line is $100 \pm 20\,\mathrm{km\,s^{-1}}$, with some component of this velocity dispersion coming from the small velocity shear.

The velocity offsets between the [O II] and transmitted Lyα emission profiles are usually interpreted in terms of a starburst-driven outflow. This model provides a good description of the integrated line emission profiles of high-redshift galaxies and more detailed observations of local starbursts (e.g. Tenorio-Tagle et al. 1999; Heckman et al. 2000; Pettini et al. 2002; Shapley et al. 2003; Grimes et al. 2006). Here, we investigate the implication for this model from the spatially resolved profile that we have observed. We base our interpretation on the specific models of Mas-Hesse et al. (2003) which assume that the spatially compact [O II] nebular emission traces the star-forming regions in the nucleus of a starbursting galaxy.

In these models, the velocity offsets between [O II] and Lyα is generated by a star-forming region embedded in an outflowing bubble. The models have been extensively investigated in local starburst galaxies where similar spatially resolved data are available. Indeed, there is strong similarity between the data we present, and the local galaxy Haro 2 studied by Mas-Hesse et al. (2003). The spatial extent (500 pc) and velocity shift ($v_{\mathrm{shell}} \sim 200\,\mathrm{km\,s^{-1}}$) seen in Haro 2 are smaller than the $z = 4.88$ galaxy, but otherwise the systems are remarkably similar. Both show Lyα emission that extends beyond the nebular emission region and both show a blue absorption cut-off to the Lyα emission line and a similar red wing. Crucially, both data sets show no detectable variation in the shape of the Lyα emission profile across the emission region. It is remarkable that this galaxy, seen 1 Gyr after the big bang is so similar to the local system at $z = 0.0049$.

The basis of the interpretation is that the starburst generates a large overpressurized region which surrounds the nebula. Within the ISM, the flow is Rayleigh–Taylor unstable so that the initial shell breaks up leaving behind denser gas clumps that may be responsible for the extended Lyα emission region. The outflow tends to break out of the galaxy along the axis of least resistance. In the case of a disc (or flattened) galaxy, this generates an approximately bi-conical outflow. When the outflow reaches the smoother, lower density gas distribution in the halo of the galaxy, a new shell develops as the outflow sweeps up material from the galaxy's halo, creating a screen between the observer and the source. As the shell travels away from the galaxy, it becomes dense enough to recombine and its Lyα opacity becomes large. Mas-Hesse et al. (2003) interpreted Haro 2 as being an example of a system in these later stages, and the $z = 5$ arc fits into the paradigm well.

The model interprets the spatially integrated properties of the emission and absorption lines seen in Fig. 6 as follows: the main peak of Lyα emission comes from photons emitted from the star-forming regions. To reach the observer, these must pass through part of the foreground (blueshifted) shell. This absorption causes the peak emission wavelength to appear redshifted relative to the nebular emission lines. In addition, photons may be scattered or emitted from the receding shell. Photons that are either created on the inner surface of the shell (e.g. by UV irradiation from the starburst), or multiply scattered within the receding shell so that they acquire the mean velocity of the shell (see the discussion of Hansen & Oh 2006) will be seen as redshifted by the observer.

However, while the integrated spectrum is certainly consistent with the presence of an outflowing bubble, it gives no indication of its physical size, or whether the bubble geometry is appropriate. For example, the integrated spectra could be equally well explained by

a large-scale outflow, or a small bubble only just surrounding the starburst region. To investigate the energy of the outflow, and its ability to escape the host galaxy's gravitational potential, we must use spatial information in our spectra.

We begin by considering the dominant contribution to the Lyα line from photons travelling directly towards the observer. The wavelength of the blue cut-off in the line is determined by the outflow velocity seen by the observer. If the bubble is spherical and close to the galaxy, we would expect to see significant variation in the blue cut-off across the emission region since the line-of-sight velocity of the outflow depends on $\sqrt{1-(b/R_s)^2}$, where b is the impact parameter and R_s is the shell radius. Clearly the consistency of the blue cut-off in Lyα across the galaxy implies that the shell is much larger than the galaxy so that the illuminated portion of the absorbing screen has a planar geometry. We illustrate the likely viewing geometry in Fig. 7 (cf. fig. 18 of Mas-Hesse et al. 2003) for an outflow in the shell recombination phase (phase 4 in their classification scheme). In Haro 2, Legrand et al. (1997) were able to estimate the size of the shell from its low surface brightness Hα emission. They estimated that the projected diameter of the shell is 2.5 kpc, around five times the diameter of the emission region. A similar ratio would seem appropriate for the arc, although the shell could obviously be larger.

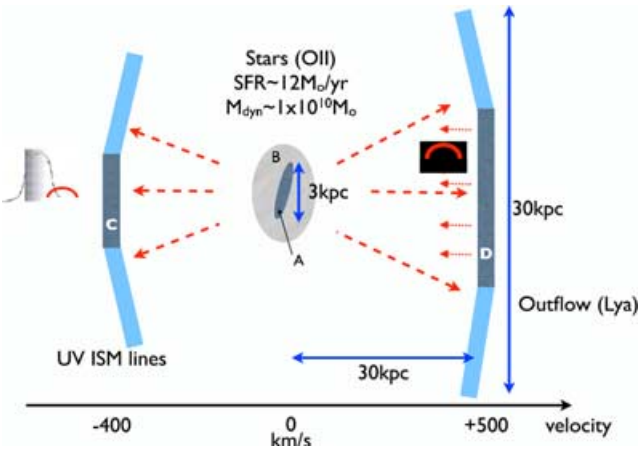

Figure 7. This figure illustrates the details of the proposed configuration to explain the spatially resolved emission spectrum. The Lyα emission comes predominantly from photons generated in the star-forming region 'A'. The Lyα emission region is physically larger than that due to recombination in dense gas clumps that have not yet been swept up and ionized by the outflow, and the resonant Lyα may not escape readily from the central regions of the starburst. The outflow cavity 'B' contains predominantly ionized material flowing out of the galaxy. It is hot and diffuse and therefore not seen directly. However, the shell 'C' (travelling towards the observer) that has formed as the wind has swept up the interior of the cavity can be seen in absorption at $-v_{\rm shell}$ against the central Lyα emission region. The geometry of the outflow, and its extent compared the source mean that the projected velocity is almost constant across the illuminated portion of the shell. Photons that scatter off the receding shell ('D'), or are produced by ionization of its inner edge by UV photons from the starburst, are seen by the observer as a weak emission line (broadened by radiative transfer effects) at $+v_{\rm shell}$. The biconical nature of the outflow is key to explaining why the redshifted emission is only seen over the portion of the shell directly behind region 'A'. Redshifted photons from other regions of the receding shell must pass through the area of the galaxy that has not yet been ionized. Even though they are redshifted relative to the galaxy, they will be absorbed since the absorbing column is likely to be extremely high. Note that photons that pass through the central ionized region of the galaxy are unlikely to be absorbed by the foreground shell since they are redshifted by $+2v_{\rm shell}$.

Our data also require an additional contribution from photons scattered or created in the receding shell. For a large spherical shell, we would expect to see a widespread low surface brightness emission at this wavelength (e.g. Fig. 7). However, no such distributed emission is seen in our data, or in Mass-Hesse et al.'s observations of local systems. Instead, by collapsing the data cube over a region dominated by the excess flux in the red wing, we find that the redshifted wing seems to have a similar angular distribution to that of the Lyα emission coming directly from the galaxy. However, we can extend the model of Mass-Hesse et al. to explain the limited spatial extent of this emission as a result of the bi-conical outflow geometry. Redshifted photons from most of the receding shell must pass through the area of the galaxy that has not yet been ionized by the starburst. Even though they are redshifted by $+v_{\rm shell}$ relative to the galaxy, they will still be absorbed since the absorbing column is likely to be extremely high. Only in the ionized region surrounding the starburst will the Lyα opacity be sufficiently low to allow photons to pass though the otherwise neutral disc (photons that pass through the ionized region are unlikely to be absorbed by the foreground shell since they are redshifted by $+2v_{\rm shell}$). The column density of the residual gas disc is also likely to be much larger than that of the expanding shell. The result of this geometry is that the redshift wing will have a spatial extent similar to that of the main Lyα line.

The proposed geometry explains the spatial distribution of the spectra without needing to invoke a special viewing angle. The only constraint is that the system is viewed down through the outflow cone. As the inclination between the outflow axis and the viewer becomes significant, we might expect to detect some rotation from the galaxy (a small shear is suggested by our SINFONI spectra of the [O II] emission); however, a shift of a several $10\,{\rm km\,s^{-1}}$ in the *intrinsic* profile of the Lyα line is unlikely to be observable since the line shape is so strongly shaped by the blueshifted absorption (which does not share the velocity shear of the galaxy). If the system is viewed at a larger angle, Lyα is likely to be completely absorbed since the expansion velocity perpendicular to the cone is small. In this case, it is unlikely that a redshift would have been obtained for this arc. It is also worth noting that the outflow spends much of its time in this post-blow-out phase. In earlier phases, the foreground shell will have lower column density or may even show emission at its leading edge; in later phases, as the shell slows down and stalls, Lyα does not escape at all. This model does not require us to be observing the galaxy at a particularly special phase of its evolution or at a special viewing angle.

Whilst the proposed bipolar outflow fits the observables, there are other possible scenarios which would explain the velocity offsets we measure: if the outflow were instead within the galaxy, and the Lyα emission were non-Gaussian (e.g. a Lorentzian), then the red wing of emission seen at $z = 4.8860$ could be explained without a receding shell. In this model, the blueshifted material could arise due to an ISM outflow which is in the process of breaking out of the galaxy. However, the constancy of the Lyα emission-line shape and centroid is difficult to explain – any velocity motion within the star-forming regions should be reflected by the Lyα, which is not seen in our data.

4.1.1 Energetics of the outflow

Although there are uncertainties in the geometry and column density of the outflowing shell, it is nevertheless interesting to consider the energetics of the outflow, in order to see if the bipolar outflow

scenario is reasonable. For a normal stellar initial mass function, supernovae provide $\sim 10^{49}$ erg per solar mass of stars (e.g. Benson et al. 2003); thus, for a galaxy with an SFR of $12 \pm 2\,M_\odot\,yr^{-1}$, $\sim 10^{50}$ erg is available per year and the maximum extent of the Lyα emission is $\sim$12 kpc diameter. We estimate the distance of the shell from the galaxy by assuming that the linear size of the region covered by the swept-up shell is at least q times the size of the maximum extent of Lyα emission region. For Haro 2, the shell is at least three times the spatial extent of the star-forming regions. If we adopt $q < 3$, then we would expect to detect variations in the velocity of foreground absorber. This suggests a linear size for the end of the cone of $\gtrsim$30 kpc. Adopting an opening angle for the outflow of $\sim 60^\circ$, we estimate that the shell must be located $\gtrsim$30 kpc from the starburst region.

At a velocity of $\sim$500 km s^{-1}, it takes 60 Myr to travel out to a distance of 30 kpc; within this time, supernovae will provide a total energy of $\sim 6 \times 10^{57}$ erg. Clearly, there are a number of uncertainties in this estimate: not least that the shell may have decelerated from an initial higher velocity which would reduce the time-scale. Nevertheless, we can estimate the mass of the outflow via $M_{\rm outflow} = N_{\rm H\,I} \times M_{\rm H}/x$, where $N_{\rm H\,I}$ is the column density, A is the area of the cone and $M_{\rm H}$ is the atomic mass of hydrogen. Adopting the value of the observed column density we derived in Section 3.2 of $N_{\rm H\,I} = 1.6 \times 10^{19}$ cm^{-2} and that the cone is uniform over an area of 700 kpc^2, the total mass of the outflow is $1.8 \times 10^8/x\,M_\odot$, where x is its H I fraction. The kinetic energy of the outflow is then $E = \frac{1}{2}mv^2 = 5 \times 10^{56}/x$ erg. Thus, the outflow is energetically feasible if the neutral fraction is greater than 10 per cent, or the column density of the shell is lower than that we have assumed. (Note, however, that these two factors well tend to play off against each other: a lower column density will tend to have a lower neutral fraction.)

It is interesting to note that the implied mass outflow rate is therefore $\sim 3/x\,M_\odot\,yr^{-1}$. If we assume $x = 0.1$, then the mass outflow rate is very efficient at ejecting baryons from the galaxy, with the mass loading of the wind being more than twice the SFR of the galaxy.

The estimates above are clearly uncertain. Nevertheless, it is interesting to see how far the expanding material might be expected to travel after the end of the starburst. We assume a halo circular velocity of 150 km s^{-1} and a wind speed of 500 km s^{-1} located 30 kpc from the centre of the halo. If the wind flows freely out of the galaxy, it is completely unbound. However, the wind will slow down dramatically if it sweeps up material. To make an estimate of how far the wind will travel, we assume that the wind expands into an Navarro–Frenk–White halo with a baryon fraction of 18 per cent and that the wind has an opening angle of 60°. Even though the wind rapidly gains mass as it expands, it reaches a minimum of 160 kpc (almost 1 comoving Mpc) before stalling. Thus, this starburst-driven wind has enough energy to pollute a volume of approximately $\sim$3 Mpc^3.

5 CONCLUSIONS

The issues of metal ejection and feedback are some of the most-outstanding problems in galaxy formation. One of the most-important recent observational breakthroughs is that most high-redshift protogalaxies appear to be surrounded by 'superwinds' which are expelling material from the galaxy disc. However, at high redshift (where star formation efficiency was at its peak and therefore this phenomenon is likely at its peak activity), observational evidence is usually based on measuring the velocity offsets between the nebular emission (such as [O II] or Hα) and rest-frame UV lines, such as Lyα or UV ISM lines. These observations are usually based on long-slit observations which lack spatial information, which is crucial if we are to understand the dynamics and fate of the outflowing gas.

In this paper, we have spatially resolved and mapped the dynamical properties of a highly magnified gravitationally lensed galaxy at $z = 4.88$. The main features are as follows.

(i) The lensing amplification is a factor of 16 ± 2 ($\Delta m = 3.0 \pm 0.2$ mag). In the (reconstructed) source-frame, the *HST* imaging suggests that the galaxy is only $\sim 2 \times 0.8$ kpc FWHM. Moreover, the lensing-corrected I-band magnitude is $I = 25.2$. For comparison, an L^* LBG at $z\sim$ has $i = 25.4$, suggesting this galaxy is typical of galaxies at these early times. Due to the lensing amplification, we are able to study a typical $z \sim 5$ galaxy at high S/N and spatially resolve the galaxy on $\lesssim$200 pc scales.

(ii) The [O II]$\lambda\lambda$3726.2,3728.9 emission line maps the (systemic) nebular emission and shows a peak-to-peak velocity gradient of $\lesssim$60 km s^{-1} across 3 kpc in projection. The integrated [O II] emission-line flux suggests an integrated SFR of $12 \pm 2\,M_\odot\,yr^{-1}$. The velocity shear, spatial extent and velocity dispersion of this nebular emission suggest a dynamical mass of $\sim 1 \times 10^{10}\,M_\odot$ within a radius of 2 kpc.

(iii) The Lyα emission is much more extended than either the UV continuum or the [O II] emission, extending over 11.9×2.4 kpc (FWHM). The Lyα emission has a asymmetric profile causing it to appear redshifted from the systemic velocity by $+200 \pm 40$ km s^{-1}. Across the whole galaxy image both the shape and the centroid of the Lyα emission are remarkably constant with the centroid of Lyα varying by $<$10 km s^{-1}.

(iv) Both the collapsed and the spatially resolved Lyα emission are best fitted with a three-component model: (1) an underlying (Gaussian) emission profile which has a redshift and width in excellent agreement with the nebular emission; (2) an absorber with a Voigt profile at -500 km s^{-1} and a column density of 1.6×10^{19} cm^2, and (3) a broad redshifted emission-line component at $+400$ km s^{-1}.

(v) In the collapsed rest-frame UV spectrum, the weak UV ISM lines of Si IV are blueshifted from the systemic velocity by -400 ± 100 km s^{-1} (the velocity of these lines are in agreement with the velocity of the absorber seen against Lyα).

The velocity offsets between the nebular emission and spatially extended Lyα are comparable to those seen in most high-redshift LBGs at similar redshifts (Shapley et al. 2003; Erb et al. 2003) and are usually attributed to galactic-scale outflows. Hence, this leads us to interpret the results in the context of an evolving starburst outflow and we illustrate the likely viewing geometry in Fig. 7. In this model, the [O II] emission is assumed to trace the underlying (star-forming) region embedded in an bi-conical outflowing bubble in which the starburst generates an overpressurized region within the ISM which becomes Rayleigh–Taylor unstable in which the initial shell breaks up, leaving behind denser clumps which may be responsible for the extended Lyα region. Any outflow will break out of the galaxy along the axis of least resistance and hence for gas in a planar or bar-like galaxy this generates an approximately bi-conical outflow.

The proposed geometry naturally explains the spatial distribution of the spectra and the velocity offsets and structures we observe. We consider the energetics of the outflow and show that the proposed model is self-consistent and energetically feasible. The energy of the wind is such that it plausibly reaches $\sim$160 kpc (almost 1 comoving Mpc) before stalling. At this point, it will have polluted a comoving volume of nearly 3 Mpc^3 with metal-enriched material.

Whilst these observations are based on a single galaxy, our results clearly show the power of combining gravitational lensing with optical and near-infrared observations to probe the star formation activity, masses and feedback processes in typical high-redshift galaxies in great detail. The next step is to generate a statistically useful sample to gauge the prevalence outflows from these young galaxies. In turn, these measurements will help us understand the widespread enrichment of the early universe, and may explain why only 10 per cent of baryons cool to form stars.

ACKNOWLEDGMENTS

We would like to thank the anonymous referee for their suggestion which significantly improved the content and clarity of this paper. We also thank Alice Shapley and collaborators for allowing us to use their rest-frame UV composite spectrum of LBGs, Markus Kissler-Patig for advice and support for the ESO/IFU observations and Tom Theuns, Howard Yee, Tracy Webb and Erica Ellingson for useful discussions. AMS acknowledges support from a PPARC fellowship, RGB acknowledges a PPARC Senior Fellowship, GPS and IS acknowledge support from Royal Society University Research Fellowships and J-PK thanks support from CNRS.

REFERENCES

Balogh M. L., Pearce F. R., Bower R. G., Kay S. T., 2001, MNRAS, 326, 1228
Baugh C. M., Lacey C. G., Frenk C. S., Granato G. L., Silva L., Bressan A., Benson A. J., Cole S., 2005, MNRAS, 356, 1191
Benson A. J., Bower R. G., Frenk C. S., Lacey C. G., Baugh C. M., Cole S., 2003, ApJ, 599, 38
Bower R. G. et al., 2004, MNRAS, 351, 63
Campusano L. E., Pelló R., Kneib J.-P., Le Borgne J.-F., Fort B., Ellis R., Mellier Y., Smail I., 2001, A&AP, 378, 394
Eisenhauer F. et al., 2003, in Iye M., Moorwood A. F. M., eds, Proc. SPIE Vol. 4841, Instrument Design and Performance for Optical/Infrared Ground-based Telescopes. SPIE, Bellingham WA, p. 1548
Ellis R., Santos M. R., Kneib J., Kuijken K., 2001, ApJ, 560, L119
Erb D. K., Shapley A. E., Steidel C. C., Pettini M., Adelberger K. L., Hunt M. P., Moorwood A. F. M., Cuby J., 2003, ApJ, 591, 101
Erb D. K., Steidel C. C., Shapley A. E., Pettini M., Reddy N. A., Adelberger K. L., 2006, ApJ, 646, 107
Fan X. et al., 2006, AJ, 132, 117
Förster Schreiber N. M. et al., 2006, ApJ, 645, 1062
Franx M., Illingworth G. D., Kelson D. D., van Dokkum P. G., Tran K., 1997, ApJ, 486, L75
Genzel R. et al., 2006, Nat, 442, 786
Gladders M. D., Yee H. K. C., Ellingson E., 2002, AJ, 123, 1
Grimes J. P., Heckman T., Hoopes C., Strickland D., Aloisi A., Meurer G., Ptak A., 2006, ApJ, 648, 310
Hansen M., Oh S. P., 2006, MNRAS, 367, 979
Heckman T. M., Lehnert M. D., Strickland D. K., Armus L., 2000, ApJS, 129, 493
Henault F. et al., 2003, in Iye M., Moorwood A. F. M., eds, Proc. SPIE Vol. 4841, Instrument Design and Performance for Optical/Infrared Ground-based Telescopes. SPIE, Bellingham, WA, p. 909
Kassiola A., Kovner I., 1993, ApJ, 417, 450
Kennicutt R. C., 1998, ARA&A, 36, 189
Kneib J., Ellis R. S., Santos M. R., Richard J., 2004, ApJ, 607, 697
Kneib J.-P., 1993, PhD thesis, Université Paul Sabatier, Toulouse, France
Kneib J.-P., Ellis R. S., Smail I., Couch W. J., Sharples R. M., 1996, ApJ, 471, 643
LeFevre O., Saisse M., Mancini D., Brau-Nogue S., Caputi O., Castinel L., D'Odorico S., Garilli B., 2003, in Iye M., Moorwood A. F. M., eds, Proc. SPIE Vol. 4841, Instrument Design and Performance for Optical/Infrared Ground-based Telescopes. SPIE, Bellingham, WA, p. 1670
Legrand F., Kunth D., Mas-Hesse J. M., Lequeux J., 1997, A&AP, 326, 929
Martin C. L., 2005, ApJ, 621, 227
Mas-Hesse J. M., Kunth D., Tenorio-Tagle G., Leitherer C., Terlevich R. J., Terlevich E., 2003, ApJ, 598, 858
Ouchi M., Shimasaku K., Okamura S., Furusawa H., Kashikawa N., Ota K., Doi M., Hamabe M., 2004, ApJ, 611, 685
Pettini M., Steidel C. C., Adelberger K. L., Dickinson M., Giavalisco M., 2000, ApJ, 528, 96
Pettini M., Rix S. A., Steidel C. C., Hunt M. P., Shapley A. E., Adelberger K. L., 2002, Ap&SS, 281, 461
Ravindranath S. et al., 2006, ApJ, 652, 963
Sand D. J., Treu T., Ellis R. S., Smith G. P., 2005, ApJ, 627, 32
Shapley A. E., Steidel C. C., Pettini M., Adelberger K. L., 2003, ApJ, 588, 65
Sharples R. M., Bender R., Lehnert M. D., Ramsay Howat S. K., Bremer M. N., Davies R. L., Genzel R., Hofmann R., 2004, in Moorwood A. F. M., Iye M., eds, Proc. SPIE Vol. 5492, Ground-based Instrumentation for Astronomy. SPIE, Bellingham, WA, p. 1179
Smail I., Dressler A., Kneib J., Ellis R. S., Couch W. J., Sharples R. M., Oemler A. J., 1996, ApJ, 469, 508
Smith G. P., Smail I., Kneib J.-P., Davis C. J., Takamiya M., Ebeling H., Czoske O., 2002, MNRAS, 333, L16
Smith G. P., Kneib J.-P., Smail I., Mazzotta P., Ebeling H., Czoske O., 2005, MNRAS, 359, 417
Steidel C. C., Shapley A. E., Pettini M., Adelberger K. L., Erb D. K., Reddy N. A., Hunt M. P., 2004, ApJ, 604, 534
Swinbank A. M. et al., 2003, ApJ, 598, 162
Swinbank A. M. et al., 2005, MNRAS, 359, 401
Swinbank A. M., Bower R. G., Smith G. P., Smail I., Kneib J.-P., Ellis R. S., Stark D. P., Bunker A. J., 2006, MNRAS, 368, 1631
Tenorio-Tagle G., Silich S. A., Kunth D., Terlevich E., Terlevich R., 1999, MNRAS, 309, 332
Teplitz H. I. et al., 2000, ApJ, 533, L65
White S. D. M., Rees M. J., 1978, MNRAS, 183, 341
Wilman R. J., Gerssen J., Bower R. G., Morris S. L., Bacon R., de Zeeuw P. T., Davies R. L., 2005, Nat, 436, 227

APPENDIX A: SERENDIPITOUS BACKGROUND GALAXIES

Since we are able to simultaneously survey all of the critical lines from $z = 0$ to 7 with the VIMOS IFU and part of the $z = 1.5$–14 critical lines with the SINFONI IFU, we exploit the SINFONI and VIMOS data to search for serendipitous sources behind the lensing cluster. We identify seven candidates between $z = 1.5$ and 5.5 from both optical and near-infrared spectroscopy, at least three of which have either optical or near-infrared broad-band counterparts. One of these sources is a radial counter-image of the $z = 4.88$ arc which is then used to provide strong constraints on the lens modelling (Section 3.1). The remaining sources in the VIMOS data cube are identified as [O II] emission at $z = 0.99$ and Lyα at $z = 3.66$. The SINFONI IFU emitters are tentatively identified as either Hα at $z =$ 1.5–2.7 or [O II] at $z \sim 5.3$ (Table A1). These observations show the power which integral field spectroscopy will have in the future in finding high-redshift galaxies behind cluster cores (e.g. Ellis et al. 2001; Kneib et al. 2004). The observations presented here also allow an insight of the deeper observations that will be made possible with even larger area integral field spectrographs on the VLT in the near future (e.g. MUSE; Henault et al. 2003 or the mosaic mode of KMOS; Sharples et al. 2004). These observations will open the doorway to probing (and spatially resolving) the properties of the primeval galaxies responsible for reionization around $z = 8$–12.

Table A1. Properties of the serendipitous sources.

ID	RA (^{h} ^{m} ^{s})	Dec. ($^\circ$ $'$ $''$)	λ_{obs} (μm)	Line flux ($\times 10^{-16}$ erg s^{-1})	Likely redshift	EW$_{observed}$ (Å)
VIMOS						
A1	02:24:33.862	−00:02:17.61	0.5665	1.4 ± 0.5	3.660 (Lyα)	470 ± 60
A2	02:24:34.602	−00:02:34.80	0.7400	6.0 ± 1.0	0.986 ([O II])	102 ± 20
R1	02:24:34.466	−00:02:34.77	0.7148	4.5 ± 0.8	4.879 (Lyα)	720 ± 30
SINFONI						
1	02:24:33.455	−00:02:21.73	2.3330	0.1 ± 0.05	2.554 (Hα)/5.259 ([O II])	>78
2	02:24:33.591	−00:02:24.22	2.2455	0.06 ± 0.03	2.421 (Hα)/5.024 ([O II])	>47
3	02:24:33.708	−00:02:25.71	1.6740	0.04 ± 0.02	1.550 (Hα)/3.159 ([O II])	>31
4	02:24:33.315	−00:02:23.28	2.4302	0.03 ± 0.02	2.702 (Hα)/5.520 ([O II])	>23

Note. Properties of the serendipitous sources in the VIMOS and SINFONI IFU fields of view.

A1 Identifying serendipitous galaxies in the data cube

Using the IFU coverage of the cluster cores, we attempt to identify serendipitous sources in the IFU data cubes. For the wavelength range of VIMOS (5000 Å–1 μm), we are able to search for Lyα between $z = 3.11$ and 6.8 and [O II] between $z = 0.34$ and 1.57. The wavelength coverage of the SINFONI IFU observations ($\lambda =$ 1.451–2.463 μm) also allow us to search for [O II] emission between redshifts $z = 2.90$ to 5.61, Hα between $z = 1.21$ and 2.75 and even Lyα between $z = 10.9$ and 19.3).

To identify serendipitous line emission, we scan each pixel of the data cube. At each wavelength in each spectrum, we calculate the noise over ±150 Å and demand an S/N of 4 to detect an emission line in at least three of the eight adjacent pixels. (We mask out any regions of strong sky emission from our analysis completely.) If line emission is detected, we then fit the emission line with a single Gaussian profile and require that the emission line must have a linewidth greater than that of the sky at the given wavelength. Using this technique, we identify three candidates in the VIMOS IFU data cube (excluding [O II], [O III] or Hβ emission from the cluster members) and four candidates in the near-infrared (SINFONI) data cube. We show the one- and two-dimensional spectra (as well as their location in the data cube) in Figs A1 and A2 and briefly review their properties and likely redshifts here.

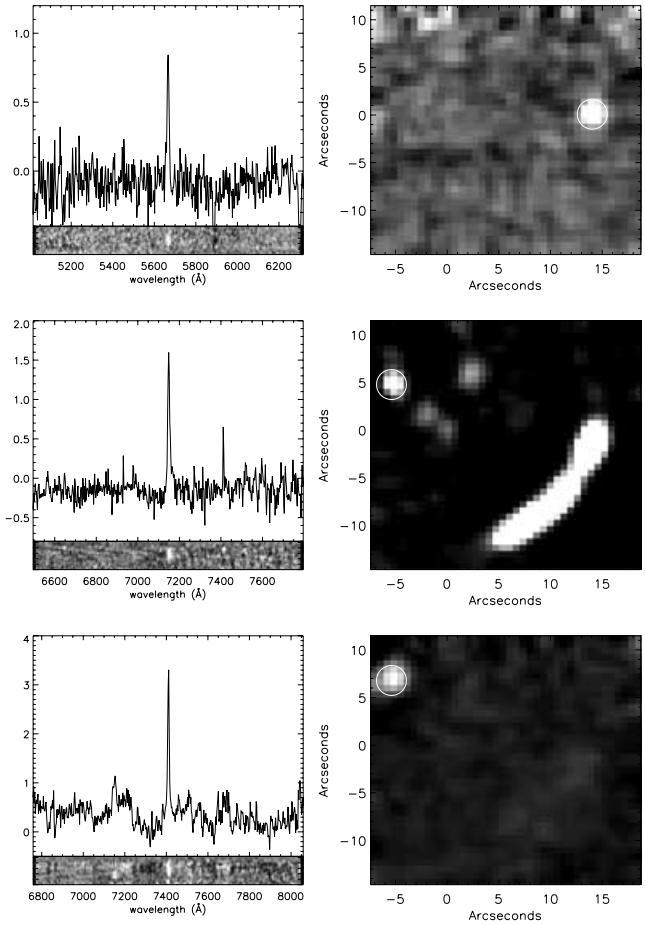

Figure A1. Spectra of the three background, serendipitous sources in the VIMOS IFU field of view. In all three panels we show the collapsed, one-dimensional spectrum, the two-dimensional spectrum (generated by unwrapping the data cube around the object) as well as the location of the object in the data cube (right-hand panel). Top panel: the superimposed foreground galaxy (labelled A1 in Fig. 1) on the third image of the $z = 4.88$ arc has strong line emission at 5600 Å which we identify as Lyα yielding a redshift $z = 3.66$. Middle panel: the $z = 4.789$ arc is a radial counter-image (labelled R1 in Fig. 1) of the arc and is used as a primary constraint on the lens model in Section 3.1. Bottom panel: the blue-disc galaxy (labelled A2 in Fig. 1) is a lensed source at $z = 0.99$ from identification of [O II] at 7400 Å.

Optical

(i) *VIMOS Source 1 (R1)*. The first serendipitous source is the radial counter-image of the $z = 4.879$ arc (labelled R1 in Fig. 1). The position of this counter-image is used as an extra constraint in the lens modelling in Section 3.1.

(ii) *VIMOS Source 2 (A1)*. In the *HST* imaging of the cluster, the third counter-image of the $z = 4.789$ arc (at approximately +6 arcsec, +14 arcsec) shows a bright knot superimposed on to the arc which does not appear in any of the other counter-images of the arc and therefore (as noted by Gladders et al. 2002) is most likely a foreground galaxy super-imposed on to the arc. This galaxy has a *V*-band magnitude of $V_{606} = 25.6 \pm 0.2$ and we identify an emission line at 5665 Å with an emission-line flux of $1.4 \pm 0.5 \times 10^{-16}$ erg s^{-1} cm^{-2} and an observed equivalent width (EW) of 700 ± 150 Å. If the line is identified as [O II], then a redshift of 0.51 yields an EW of ∼470 Å, which is high compared to local star-forming galaxies. We therefore suggest that the emission is Lyα at a redshift of $z = 3.66$ with a rest-frame EW of 150 ± 50 Å. The emission linewidth (FWHM = 12.5 Å) suggests a linewidth of 220 ± 60 km s^{-1}.

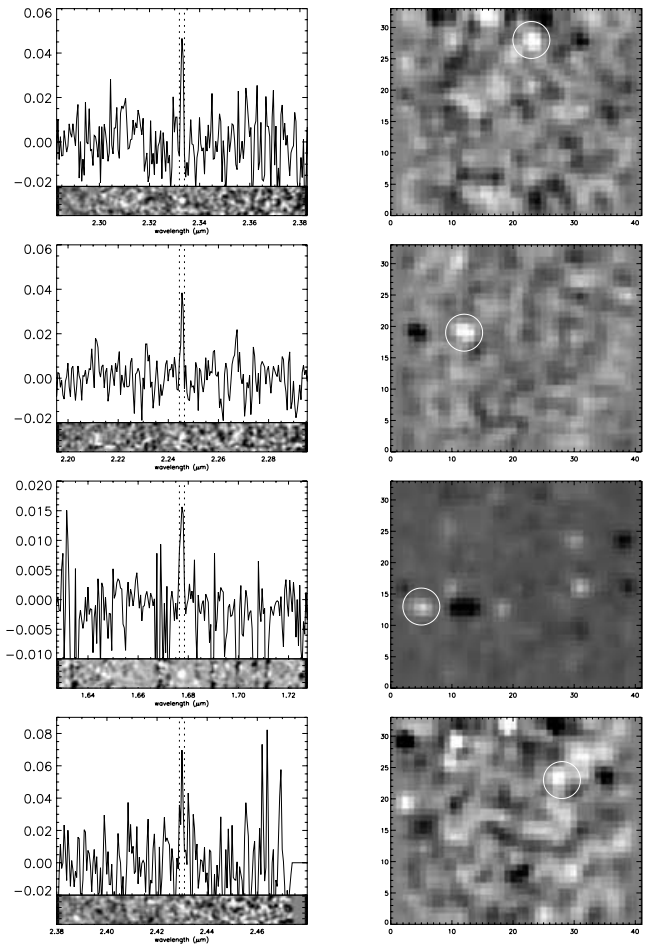

Figure A2. Spectra of the four background, serendipitous sources in the SINFONI IFU field of view. In the left-hand panels, we show the one-dimensional spectra with the two-dimensional spectra below. In the right-hand panel, we show the two-dimensional (narrow-band) images which show the positions in the data cubes for these sources. The positions of these sources are also shown in Fig. 1 and details are also given in Table A1. The images in the right-hand panel are generated by collapsing the data cubes over the wavelength range shown by the two dashed lines in the one-dimensional spectra.

(iii) *VIMOS Source 3 (A2)*. The third background galaxy detected is the blue disc-like galaxy labelled A2 in Fig. 1. We detect strong emission at 7409 Å but no other significant ($>5\sigma$) emission lines in the one-dimensional spectrum. The emission line also has a velocity shear of $\sim$5 Å across the $\sim$1.5 arcsec. If the emission is identified as [O II]λ3727, a redshift of 0.9855 is derived, placing the galaxy behind the cluster, and probably lensed. However, it is also possible that the emission is Hα at $z = 0.129$, although we place limits on the emission-line ratios of Hα/H$\beta > 12$ and Hα/[O III]λ5007 > 6. Identification as [O III]λ5007 is ruled out due to the non-detection of [O III]λ4959. Alternatively, if the emission is Hβ at $z = 0.524$, we constrain the emission-line flux ratios as Hβ/[O III]λ5007 > 8 and Hβ/[O II]λ3727 > 17. We therefore suggest the most likely identification is [O II]λ3727 at $z = 0.9855$.

Near-infrared

(i) *SINFONI Source 1*. The proximity of this source to the $z = 4.88$ critical line makes it more likely to be [O II] for $z = 5.25$. We cannot rule out Hα at $z = 2.55$, although the lack of [O III] or Hβ at 1.8 μm (although near to the atmospheric *H*-band absorption) or [N II]λ6583 emission makes it more likely [O II].

(ii) *SINFONI Source 2*. This source lies close to the high-amplification lines for $z = 2$–3 and therefore we suggest Hα is the most likely line identification. There is no strong [O III] in the *H* band.

(iii) *SINFONI Source 3*. The proximity to the $z \sim 1.5$ critical lines makes it more likely to be Hα than high-redshift [O II].

(iv) *SINFONI Source 4*. This is the weakest emission line in the sample, although it still fulfils the selection criterion. The most likely line identification is [O II] at $z = 5.51$ due to its proximity to the $z \sim 5$ critical curve. This emission line could also be identified at Hα for $z = 2.70$, however, we note that there are no signs of strong [O III] with a flux ratio limit of [O III]/Hα emission-line ratio $\lesssim$0.2.

APPENDIX B: SPECTROSCOPIC PROPERTIES OF THE CLUSTER GALAXIES

Table B1 gives the spectroscopic properties (RA, Dec., [O II] emission-line flux, linewidth (FWHM) and EW of the cluster galaxies.

Table B1. Spectroscopic Properties of the Cluster Galaxies.

ID	RA ($^{\rm h}$ $^{\rm m}$ $^{\rm s}$)	Dec. ($^\circ$ $'$ $''$)	z	Features	[O II] flux ($\times 10^{-17}$erg cm^{-2} s^{-1})	[O II] FWHM (Å)	EW (Å)
CG1	02:24:34.097	−00:02:30.90	0.7784	H&K	–	–	
CG2	02:24:34.246	−00:02:32.54	0.7725	H&K	–	–	
CG3	02:24:34.184	−00:02:31.29	0.7603	[O II]	8.5 ± 1.0	5.7	7.0
CG4	02:24:34.717	−00:02:35.22	0.7845	[O II]	12.0 ± 1.0	7.0	8.2
CG5	02:24:34.751	−00:02:28.75	0.7864	H&K, [O II]	10.0 ± 2.0	4.1	22.0
CG6	02:24:34.472	−00:02:27.71	0.7848	H&K, [O II]	20.0 ± 1.0	11.1	17.0

Notes. Properties of the BCGs, as measured from our VIMOS IFU observations. EWs and emission-line FWHM are given in the rest frame of the galaxy.

This paper has been typeset from a TEX/LATEX file prepared by the author.